

# Microwave seeding time crystal in Floquet driven Rydberg atoms

Bang Liu<sup>1,2</sup>, Li-Hua Zhang<sup>1,2</sup>, Yu Ma<sup>1,2</sup>, Tian-Yu Han<sup>1,2</sup>, Qi-Feng Wang<sup>1,2</sup>, Jun Zhang<sup>1,2</sup>, Zheng-Yuan Zhang<sup>1,2</sup>, Shi-Yao Shao<sup>1,2</sup>, Qing Li<sup>1,2</sup>, Han-Chao Chen<sup>1,2</sup>, Ya-Jun Wang<sup>1,2</sup>, Jia-Dou Nan<sup>1,2</sup>, Yi-Ming Yin<sup>1,2</sup>, Dong-Sheng Ding<sup>1,2,†</sup>, and Bao-Sen Shi<sup>1,2</sup>

<sup>1</sup>Key Laboratory of Quantum Information, University of Science and Technology of China, Hefei, Anhui 230026, China. and

<sup>2</sup>Synergetic Innovation Center of Quantum Information and Quantum Physics, University of Science and Technology of China, Hefei, Anhui 230026, China.

(Dated: April 19, 2024)

Crystal seeding enables a deeper understanding of phase behavior, leading to the development of methods for controlling and manipulating phase transitions in various applications such as materials synthesis, crystallization processes, and phase transformation engineering. How to seed a crystalline in time domain is an open question, which is of great significant and may provide an avenue to understand and control time-dependent quantum many-body physics. Here, we utilize a microwave pulse as a seed to induce the formation of a discrete time crystal in Floquet driven Rydberg atoms. In the experiment, the periodic driving on Rydberg states acts as a seeded crystalline order in subspace, which triggers the time-translation symmetry breaking across the entire ensemble. The behavior of the emergent time crystal is elaborately linked to alterations in the seed, such as the relative phase shift and the frequency difference, which result in phase dependent seeding and corresponding shift in periodicity of the time crystal, leading to embryonic synchronization. This result opens up new possibilities for studying and harnessing time-dependent quantum many-body phenomena, offering insights into the behavior of complex many-body systems under seeding.

Crystal seeding is a fundamental process used in the field of crystallography to facilitate the controlled growth of crystals [1, 2]. By introducing preformed crystals, either of the same or different composition, into a crystallizing solution, nucleation and growth of new crystals can be initiated and guided [3]. This step has proven to be crucial in optimizing the crystallization process, enabling the production of high-quality crystals with desired properties. The addition of seed crystals provides a template for the newly forming crystals to align and grow upon. For example, the nucleation of ice involves the formation of a small ice nucleus, known as an ice embryo or seed, from a supercooled liquid or vapor phase, around which additional water molecules can attach and grow into larger ice crystals [4].

In recent years, a fascinating crystal in time domain was put forward called as “time crystal” in the field of physics [5], exhibiting non-equilibrium properties and temporal periodicity. Time crystals are the exotic non-equilibrium states that break time-translation symmetry in both discrete and continuous ways [6–9], and are widely studied in experiments [10–18] and theories [19–24] in different systems. Researchers are actively exploring the exotic properties of time crystals beyond the realm of fundamental physics [25–33], which deepen our understanding of time crystals. The emergence of time crystals relies on carefully engineered interactions between individuals. The many-body interactions are of utmost importance in enabling and sustaining the unique properties observed in time crystals. By periodically driving the system, typically through the application of external fields or laser pulses, the particles are forced into a cyclic motion that breaks the time-translation symmetry.

The long-range interaction offered by Rydberg atoms provides a good platform for study of the non-equilibrium dynamics [34–36] in many-body physics. The observed oscillation possess a certain degree of order and behavior that goes against the expected behavior dictated by the second law of thermodynamics, allowing us to study discrete and continuous time crystals [36–38]. Due to their unique nature, it is intriguing to see how to seed time crystals as the same way as traditional crystals. Recently, a theoretical work [39] introduces the concept of seeding time crystal, where a single subsystem in a broken-symmetry phase acts as a nucleation center, inducing time-translation symmetry breaking throughout the ensemble. Once time crystal nucleation begins, it triggers the growth of time crystals, leading to the formation of larger time crystal structures.

In this work, we have experimentally realized seeding discrete time crystal (DTC) in strongly interacting Rydberg atoms under external radio-frequency (RF) field periodic driving conditions. By applying an amplitude modulated microwave field to periodically driving Rydberg atoms, we build a crystalline order that serves as a seed, causing time-translation symmetry breaking throughout the entire ensemble. The features of the seeded time crystal are closely connected to variations in the seed, leading to synchronized subharmonic dynamics. This seeding method enables the adjustment

† dds@ustc.edu.cn

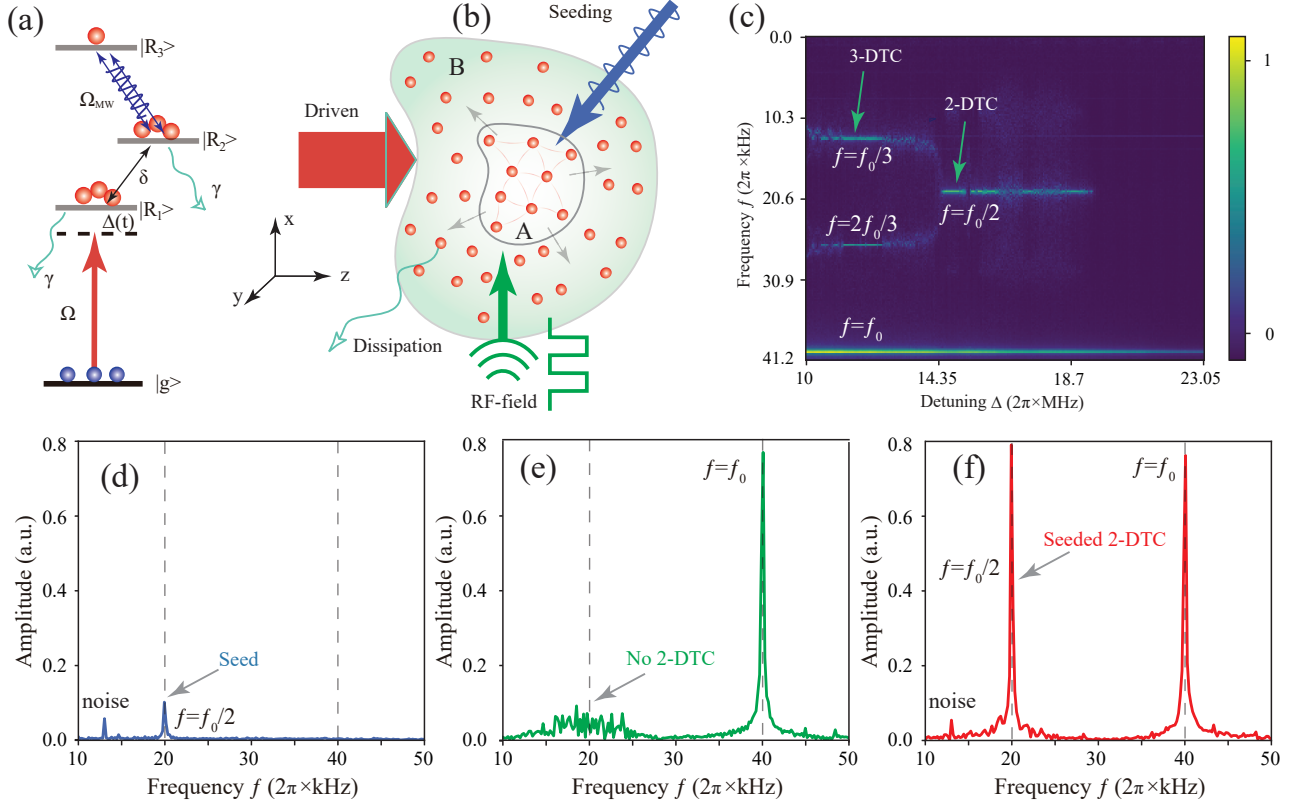


Figure 1. **Physical model of seeding time crystal.** (a) Energy level diagram, which includes a ground state  $|g\rangle$  and Rydberg states  $|R_{1,2}\rangle$ , the detuning  $\Delta(t)$  can be shifted periodically by applying an external pulsed radio-frequency (RF) field, both of Rydberg states have a decay rate of  $\gamma$ . A laser drives the atom ground state  $|g\rangle$  to  $|R_{1,2}\rangle$  with Rabi frequency  $\Omega_{1,2}$ , and another amplitude modulated microwave field couples the states  $|R_2\rangle$  and  $|R_3\rangle$  with a Rabi frequency  $\Omega_{MW}$ . (b) Physical diagram containing seeding time crystal in a system composed of driven and dissipation Rydberg atoms and the driving RF field. The microwave field driving creates a seed of breaking time translation symmetry in subspace (labeled by A), and then growing as a global time crystal of the entire ensemble (labeled by B). (c) Measured phase maps of no-DTC, 2-DTC, 3-DTC, and their transitions. The color bar represents the Fourier transform intensity. (d-f) The measured Fourier spectrum of input seed signal without RF field (d), Fourier spectrum with absent of seed signal (e), and Fourier spectrum with both of inputting seed signal and RF field (f). The weak signal on the left side of the spectrum is the system noise.

of the seeded subharmonic response frequency and the phase. By changing the frequency of the seed, we alter the underlying temporal arrangements, resulting in different time crystal formations beyond the integer DTCs. The reported results on seeding time crystal open up new avenues for controlling of non-equilibrium physics and allowing for the controlled growth of time crystals with desired properties.

### Physical Model and Experimental Diagram

To demonstrate the physical concept of seeding time crystal, we first build a quantum many-body system with periodic Floquet driving, in which the system can produce DTCs [38]. The system energy diagram is depicted by Fig. 1(a), which contains  $N$  atoms consisting of ground state  $|g\rangle$  and Rydberg states  $|R_{1,2}\rangle$ . By applying square wave modulation to the detuning  $\Delta(t) = \Delta_0 + \Delta$

when  $0 \leq t < T/2$ , and  $\Delta(t) = \Delta$  when  $T/2 \leq t < T$ , thus this system satisfies discrete time translation symmetry under this periodic Floquet driving. To demonstrate the process of seeding time crystal, an amplitude modulated microwave field with a modulated frequency of  $f_s$  is used to drive the Rydberg states between  $|R_2\rangle$  and  $|R_3\rangle$ . Here,  $|R_3\rangle$  is used as an auxiliary state for seeding. The physical diagram is represented in Fig. 1(b). In this physical diagram, the state of broken symmetry in subspace A induced by the microwave driving gives rise to unique properties and behaviors. This broken symmetry phase serves as a seed, initiating a cascade effect that gradually spreads throughout the ensemble. As the cascade progresses, the global time crystal in subspace B emerges, manifesting as a synchronized oscillation or repetition of physical properties over time. In this process, as the number of state spaces with  $N$  interacting  $m$ -level atoms have  $m^N$  state spaces (here  $m = 3$  for the model), the presence of weak microwave field peri-

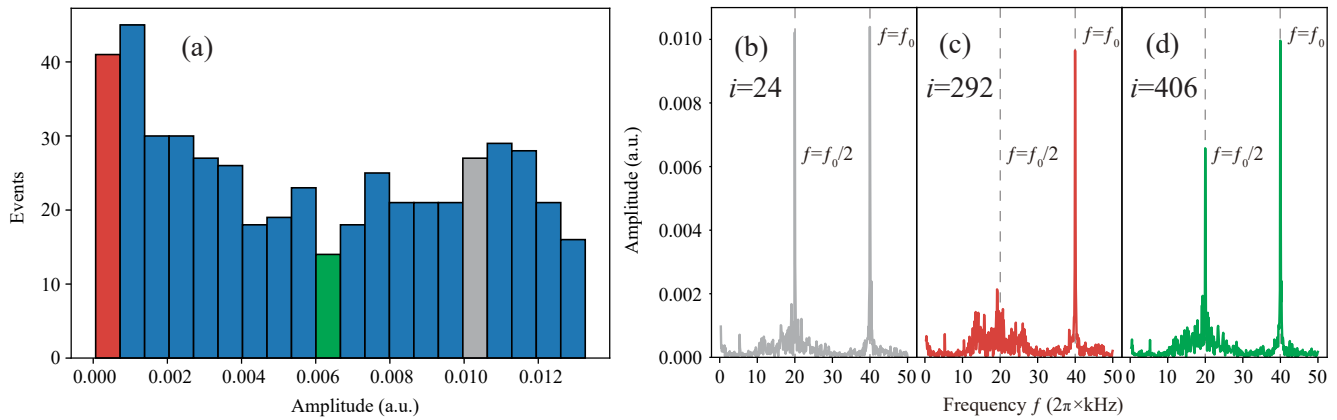


Figure 2. **Random 2-DTC orders seeding.** (a) Histogram of the amplitude of 2-DTC acquired from  $i = 1 \sim 500$  independently experimental trials. In these measurements, the relative phase between the seed field and the RF-field is fixed. (b-d) The examples for illustrating the Fourier spectrum within the corresponding regimes shown in (a) [see red, green, and gray bars]. The measured Fourier spectrum for each example corresponds to a specific experimental trial, with  $i$  values of 24 (b), 292 (c), and 406 (d), respectively.

odic driving modifies the Rydberg population  $\rho_{R_2 R_2}$  corresponding to the subspace of the system consisting of  $N$  states.

The Hamiltonian of seeding DTC is based on periodical double Rydberg state model with additional microwave driving [36, 38]:

$$\begin{aligned}
 \hat{H}(t) = & \frac{1}{2} \sum_i \left( \Omega_1 \sigma_i^{gR_1} + \Omega_2 \sigma_i^{gR_2} + \Omega_{\text{MW}}(t) \sigma_i^{R_2 R_3} + h.c. \right) \\
 & - \sum_i \left( \Delta(t) n_i^{R_1} + (\Delta(t) + \delta) n_i^{R_2} + (\Delta(t) + \delta) n_i^{R_3} \right) \\
 & + \sum_{i \neq j} V_{ij} \left[ n_i^{R_1} n_j^{R_2} + n_i^{R_2} n_j^{R_3} + n_i^{R_1} n_j^{R_3} \right. \\
 & \left. + \frac{1}{2} (n_i^{R_1} n_j^{R_1} + n_i^{R_2} n_j^{R_2} + n_i^{R_3} n_j^{R_3}) \right]
 \end{aligned} \tag{1}$$

where  $\Omega_{\text{MW}}(t) = A_0 + A \sin(2\pi f_s t + \varphi_0 + \varphi)$  ( $f_s$  is the modulated frequency,  $\varphi_0$  is the initial phase,  $\varphi$  represents the relative phase between RF-field and seed field.),  $\sigma_i^{gr}$  ( $r = R_1, R_2$ ) represents the  $i$ -th atom transition between the ground state  $|g\rangle$  and the Rydberg state  $|r\rangle$ ,  $n_i^{R_1, R_2, R_3}$  are the population operators for the two Rydberg energy levels  $|R_1\rangle$ ,  $|R_2\rangle$  and  $|R_3\rangle$ , and  $V_{ij}$  are the interactions between the Rydberg atoms.

When  $\Omega_{\text{MW}} = 0$ , the system has discrete time translation symmetry breaking with the presence of the periodic detuning  $\Delta(t)$ , resulting in exotic phase diagram including 2-DTC, higher-order DTC, and the criticality [38]. In this work, we demonstrate the seeding operation before the criticality and observe the system subharmonic dynamics. The seeding effect is based on critical slowing down which makes the system highly sensitive to perturbations in the vicinity of the critical point. The seeded DTC occurs because of the presence of weak microwave

field periodic driving, in which it acts as a seed to trigger the subharmonic response of the many-body system.

In the experiment, we applied a three-photon electromagnetically-induced transparency (EIT) scheme to prepare the Rydberg atoms [from the ground state  $|6S_{1/2}\rangle$  to the Rydberg state  $|49P_{3/2}\rangle$  using three lasers with wavelengths of 852 nm (probe), 1470 nm, and 780 nm], and measured the Rydberg atom population by the transmission of the probe field [40, 41]. The microwave field couples the Rydberg states  $48 |D_{5/2}\rangle$  and  $49 |P_{3/2}\rangle$ , acting as a seed to trigger DTC. We firstly measure the phase diagram without the seed field, which is given in Fig. 1(c). In Fig. 1(c), the 2-DTC, 3-DTC phases and the criticality can be observed versus the laser detuning  $\Delta$ . When the system approaches criticality, the response bifurcated into no-DTC and 2-DTC (or 2-DTC and 3-DTC) phases.

In the vicinity of the critical point, the system is sensitive to the perturbations due to the critical slowing down, and even small perturbations can have a large impact on the system's behavior. We input a seed signal with a frequency of  $f_s = f_0/2$  [see Fig. 1(d)] at  $\Delta$ , this condition is before the onset of the phase transition from 3-DTC to 2-DTC. Before the critical point, there is no obvious subharmonics response in the Fourier spectra, as given in Fig. 1(e). When seeding a weak microwave signal, 2-DTC appears, see the results in Fig. 1(f). In this case, the measured ratio of output to input is greater than 7, exhibiting amplification of the seed signal.

### Random 2-DTC Orders Seeding

Near the critical point, the system is disordered and has a tendency to undergo spontaneous time-translation symmetry breaking. This leads to multiple possible non-

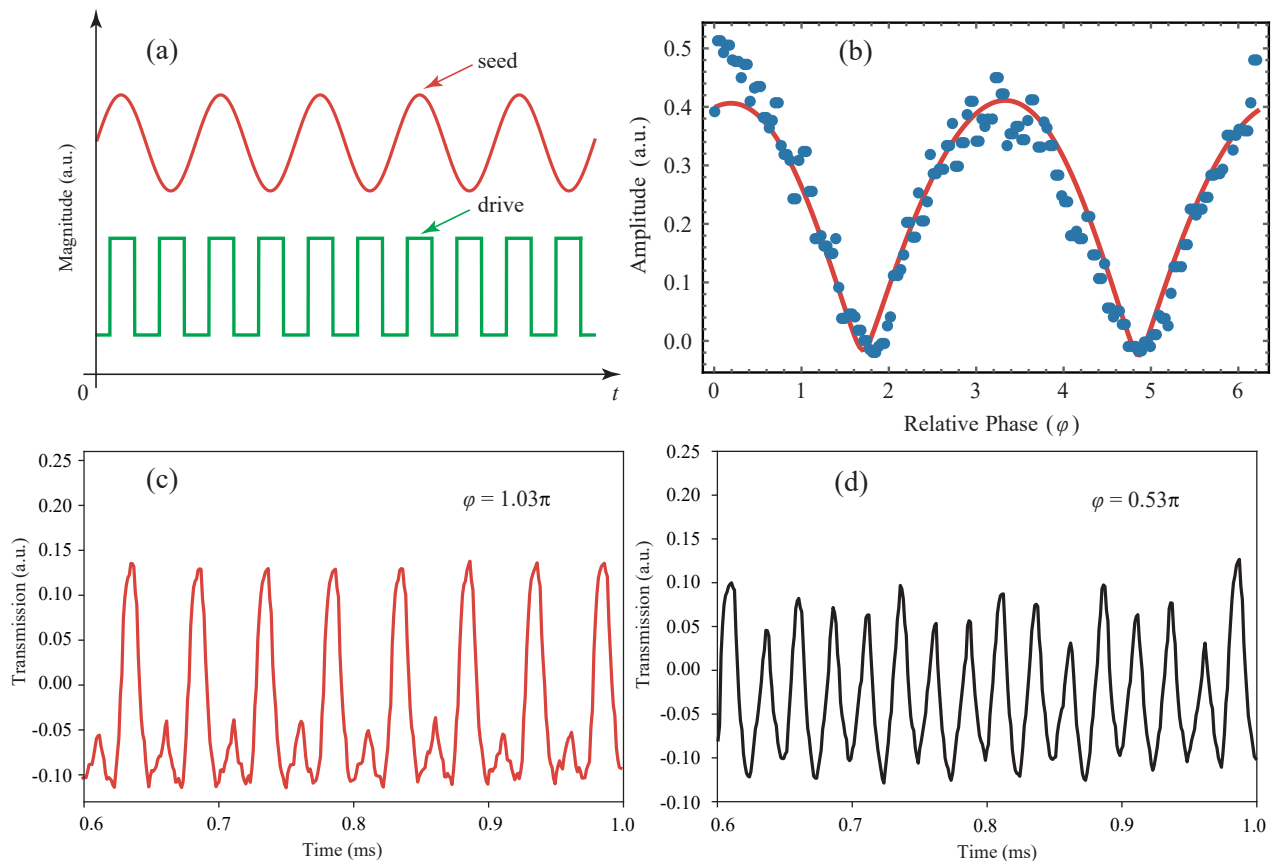


Figure 3. **Phase-locked seeding.** (a) The time sequence of the driving RF-field (green) and the microwave seed field (red). The seed has a sinusoidal function and the RF-driver is a TTL signal. In this case, the periodicity of the seed is twice of the driving. The measured amplitude of 2-DTC (solid dots) versus the relative phase  $\varphi$  between the driving field and the seed field. The red curve is the theoretical fit. (c) and (d) are the measured responses with relative phases  $\varphi = 1.03\pi$  and  $\varphi = 0.53\pi$ .

equilibrium states, referring to disordered DTC phases. When the seed field is applied, the system can follow different trajectories and choose different non-equilibrium states, resulting in randomization of the phase of the atoms. Due to small differences and uncertainties in each experiment, different non-equilibrium states can be achieved, which in turn affects the phase difference. By repeatedly seeding process with 500 times, we measure the amplitude of seeded harmonic response and plot histogram of the resulting non-equilibrium states. Figure. 2(a) shows the corresponding histograms of the amplitude of 2-DTC for all possible non-equilibrium states that highlight the randomization in the statistical distribution. The random counting statistics confirms the disordered phases before the criticality.

We show three examples to illustrate this randomization, see the measured results presented in Figs. 2(b-d). Figures. 2(b-d) display the Fourier spectrum at the experimental trial  $i = 24, 292,$  and  $406,$  respectively. The amplitude of the seeded 2-DTC is randomized with each trial, while the phase remains preserved for an extended period after the seeding operation. These seeded non-equilibrium states occur diverse due to the fluctuations

near the critical point.

### Phase-Locked Seeding

The emergence of the seeded 2-DTC phase is influenced by relative phase between the seed field and the RF-driving field. To illustrate this, we introduce a seed signal with a double periodicity ( $f_s = f_0/2$ ) into the microwave field and vary the relative phase  $\varphi$  after the seeding operation, as shown in Fig. 3(a). The seed field builds up a transition channel between Rydberg states  $48 |D_{5/2}\rangle$  and  $49 |P_{3/2}\rangle$ , modifying the system states in the subspace. As the intensity of the seed field varies sinusoidally, the population at the Rydberg state  $49 |P_{3/2}\rangle$  also undergoes periodic evolution. This periodic decrease in population acts as a trigger for the system to transition into 2-DTC phase. In this case, synchronization occurs, leading to the formation of a coherent and time-ordered pattern in the system.

By varying the relative phase  $\varphi$  from  $0$  to  $2\pi$ , we record the amplitude of seeded 2-DTC phase, the results are given in Fig. 3(b). During the change phase, the chang-

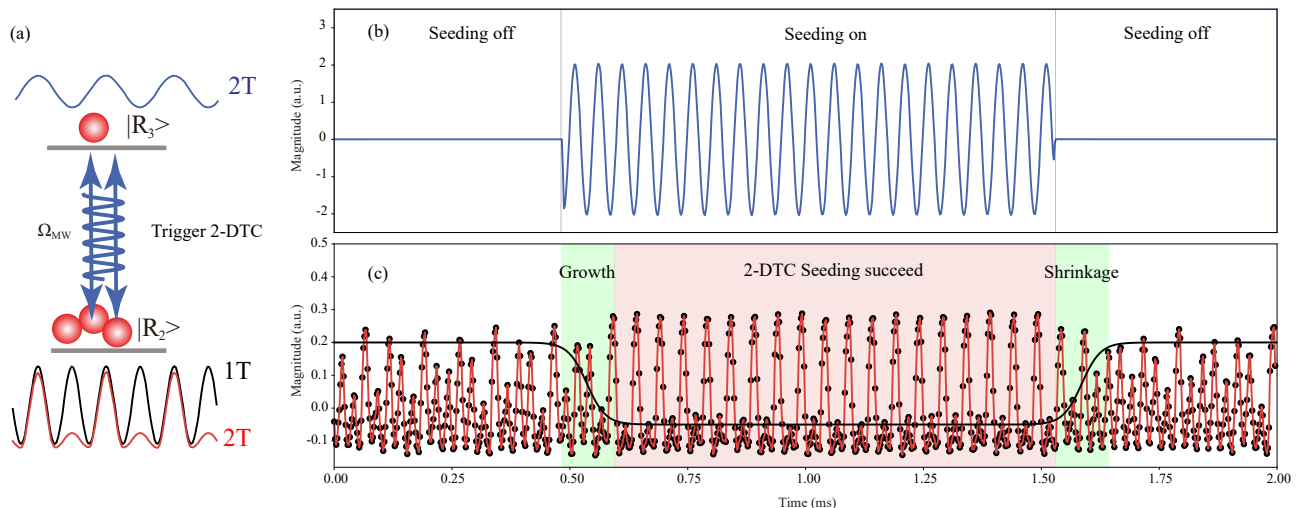


Figure 4. **2-DTC seeding dynamics.** (a) Physical diagram for triggering 2-DTC. The frequency of driving the Rydberg states  $|R_2\rangle$  and  $|R_3\rangle$  is twice the frequency of the RF-field driving. The emergence of 2-DTC is triggered by switching the microwave field on. (b) The time sequence of the microwave seed field. The seeding is initiated by switching on the microwave field. (c) The recorded transmission dynamics. The transmission dynamics can be divided into three regimes: the growth regime, the successful seeding regime, and the shrinkage regime.

ing seed waveform and the RF-driving waveform start to align with each other, causing them to overlap and leading to a joint action on exciting atoms. This joint action induces a new period of collective dynamics, thus resulting in seeded 2-DTC, see more details in Method Sections. The response of seeded 2-DTC versus  $\varphi$  behaves as a doubling frequency with relative to the seed field. For example, when  $\varphi = 1.03\pi$ , the 2-DTC phase can be amplified and we can thus observe the visible periodic doubling signal [see Fig. 3(c)], resulting in synchronization. While at  $\varphi = 0.53\pi$ , the 2-DTC phase cannot be amplified, corresponding to unsynchronization.

### Seeding Dynamics

To demonstrate the seeding dynamics, we input a pulsed amplitude modulated microwave field [with a frequency of  $f_s = f_0/2$ ] to switch the seeding field off and on. The physical diagram for illustrating seeding process is given in Fig. 4(a), where we have two Rydberg states denoted as  $|R_2\rangle$  and  $|R_3\rangle$ . The pulsed seeding field drives transition between these two states periodically. This pulsed transition process acts as a pulsed seed to affect the temporal arrangements of Rydberg population  $\rho_{R_2R_2}$  in the presence of RF-field periodic driving. Specifically, it leads to the response frequency of Rydberg population  $\rho_{R_2R_2}$  changing from  $f_0$  to  $f_0/2$  when switching the seed field on. We can then observe the seeding dynamics of time crystal by recording the probe transmission, as shown in Figs. 4(b) and (c).

In Figs. 4(b) and (c), we observe that there are gradually modified temporal arrangements of transmission at the beginning of switching, indicating the seeding growth

regime. The duration of this growth regime in our experiment is approximately  $\sim 0.1$  ms, as indicated by the shaded green area around  $t = 0.5$  ms. Once the growth regime is completed, 2-DTC is successfully seeded, as shown by the shaded red area in Fig. 4(c). In this regime, the system exhibits persistent periodical oscillation, but with the same frequency as the seed field. When we switch off the seed field, 2-DTC phase gradually disappears. This gradual decrease corresponds to the shrinkage of the seeded 2-DTC.

### Embryonic Synchronization

Furthermore, the shape and intensities of the initial seeding also influence the evolution of many-body system, leading to the emergence of DTCs with distinct frequencies. Firstly, we measure the magnitude of 2-DTC response by altering the intensities of seed field [here, we set  $f_s = f_0/2$ ]. The results are shown in Fig. 5(a). The magnitude of 2-DTC response in the Fourier spectrum is directly proportional to the amplitude of seed field  $U$ . By this way, we can effectively control the strength of seeded 2-DTC phase.

The fundamental frequency  $f_0/2$  of 2-DTC is associated with the characteristic oscillation or periodicity of time crystal's phases or patterns. When the driving frequency matches this resonant frequency, the system can synchronize its behavior with the external driving, leading to the emergence of a time crystal. When the seeding frequency deviates from  $f_0/2$ , the non-resonant seeding introduces perturbations or disruptions to the system, causing it to explore a broader range of possible energy states or patterns of oscillation, for example, fractional

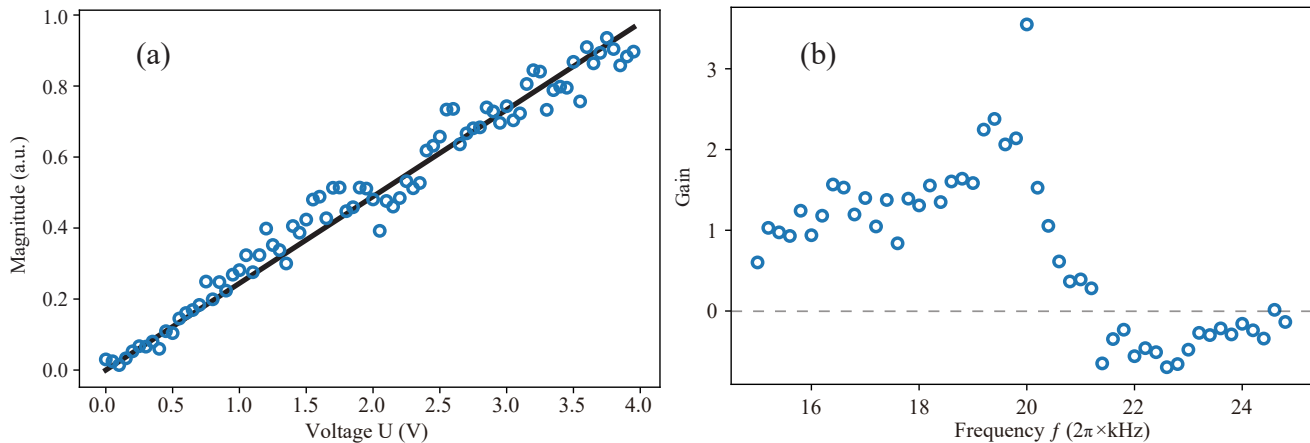


Figure 5. **Embryonic synchronization.** (a) Measured 2-DTC response versus the seed field amplitude  $U$  (blue dots). The black line is the fit linear function. Here, the seed frequency is set at  $f_s = f_0/2$ . (b) Measured gain by seeding different DTCs with altering different  $f_s$ . Notably, we observe that the subharmonics align with the seed frequency. There is a higher gain at frequencies above  $f_s$  and a weaker response at frequencies below  $f_s$ . In these cases, the relative phase  $\varphi = 1.03\pi$ .

DTCs.

Secondly, by varying the seed frequency  $f_s$  from  $2\pi \times 15$  kHz to  $2\pi \times 25$  kHz, we record the intensity of signal at frequency  $f_s$  in the Fourier spectrum. We analyze their characteristics through the magnitude of subsequent subharmonics response in the Fourier spectrum. Importantly, we observe that the subharmonics align with the frequency of seed field, resulting in embryonic synchronization, the measured data for gain of output to input are given in Fig. 5(b). The gain has a formula of  $G = (S_{\text{out}} - S_{\text{in}})/S_{\text{in}}$ , in which  $S_{\text{in(out)}}$  represents the amplitude at  $f = f_s$  in Fourier spectrum without (with) RF-field. Interestingly, we not only observe a gain greater than 0 at  $f_s = f_0/2$ , but we also find that this gain can occur for frequencies other than  $f_0/2$ . For example, when we set  $f_s = 2\pi \times 19.6$  kHz [corresponding to a non-integer DTC], we still observe a gain greater than 0. For  $f_s \neq f_0/2$  (corresponding to seeding time crystal with different embryos), we are essentially starting the system off with different starting points, which can lead to the emergence of time crystals with distinct characteristics, see Method Sections for more details. This indicates that seeded DTC response is not limited to a specific frequency and can occur at different frequencies, offering more flexibility in controlling and amplifying the signal. This variation in frequency allows us to modify the underlying temporal arrangements and ultimately obtain different types of time crystal formations.

Furthermore, we observe that the gain is not symmetric at  $f_s = f_0/2$ . The gain is present for frequencies  $f_s$  below  $f_0/2$ , but it disappears for frequencies  $f_s$  above  $f_0/2$ , resulting in a loss. This asymmetric behavior can be explained from the stimulated amplification of seeding in two energy levels [ $f = 0$  and  $f = f_0/2$ ] involved in the amplification process. In the case of  $f_s < f_0/2$ , the energy of seed field is lower than the energy difference between the two energy levels. As a result, the system is

injected with energy through the RF-driving and amplify the seed field, leading to a gain in the overall output. On the other hand, when  $f_s > f_0/2$ , the frequency of the seed field is higher than half the resonant frequency  $f_0$ . This means that the energy of seed field is higher than the energy difference between the two energy levels, and thus the system is hard to synchronize to the change of seed field. In this case, a part of Rydberg atoms are driven by the RF-field, thus the response induced by the seed field becomes weak, leading to a loss or attenuation.

## Discussions

In summary, we have studied seeding crystal in time domain in Floquet driven Rydberg atoms. The coherent driving on Rydberg atoms by the microwave field forms a nucleation center, acting a seed of broken-symmetry phase in subspace. Through the interaction of Rydberg atoms, the laser driving and dissipation, and the seed of microwave driving, the subspaces of system are coupled to each other, resulting in time-translation symmetry breaking throughout the entire ensemble. To our best knowledge, the findings in this work reveal a first experimental demonstration of seeding DTC. This work is different from seeding continuous time crystal proposed in the theoretical work [39]. The same things in these two works reveal that time crystal can be seeded in both in discrete and continuous cases. We also find that the system can be seeded at a frequency that does not match the natural resonance of 2-DTC. This variation in frequency allows us to modify the underlying temporal arrangements and ultimately obtain different types of time crystal formations, providing a avenue to study fractional DTCs. This also allows us to study and understand how the manipulation of the initial conditions influences the

behavior and properties of the resulting time crystal formation.

The introduced technological method opens up new avenues of engineering of time crystals, unlocking for the control and manipulation temporal patterns and subharmonic responses in quantum many-body systems. Furthermore, exploring the range of frequencies for generating DTCs and the phase-locking mechanism help us gain a deeper understanding of the underlying mecha-

nisms involved in their formation and stability. This achievement not only advances our fundamental understanding of time crystals but also has significant implications for various applications, such as quantum computing and quantum many-body physics. Seeding time crystals opens up exciting possibilities for further investigation on non-equilibrium quantum physics, marking a significant milestone to understand and utilize their unique properties.

- 
- [1] A. A. Chernov, *Modern crystallography III: crystal growth*, Vol. 36 (Springer Science & Business Media, 2012).
- [2] B. R. Pamplin, *Crystal Growth: International Series on the Science of the Solid State* (Elsevier, 2013).
- [3] E. A. Stura and I. A. Wilson, Analytical and production seeding techniques, *Methods* **1**, 38 (1990).
- [4] B. Murray, D. O'sullivan, J. Atkinson, and M. Webb, Ice nucleation by particles immersed in supercooled cloud droplets, *Chemical Society Reviews* **41**, 6519 (2012).
- [5] F. Wilczek, Quantum time crystals, *Physical Review Letters* **109**, 160401 (2012).
- [6] K. Sacha and J. Zakrzewski, Time crystals: a review, *Reports on Progress in Physics* **81**, 016401 (2017).
- [7] D. V. Else, C. Monroe, C. Nayak, and N. Y. Yao, Discrete time crystals, *Annual Review of Condensed Matter Physics* **11**, 467 (2020).
- [8] P. Kongkhambut, J. Skulte, L. Mathey, J. G. Cosme, A. Hemmerich, and H. Keßler, Observation of a continuous time crystal, *Science* **377**, 670 (2022).
- [9] M. P. Zaletel, M. Lukin, C. Monroe, C. Nayak, F. Wilczek, and N. Y. Yao, Colloquium: Quantum and classical discrete time crystals, *Reviews of Modern Physics* **95**, 031001 (2023).
- [10] J. Zhang, P. W. Hess, A. Kyprianidis, P. Becker, A. Lee, J. Smith, G. Pagano, I.-D. Potirniche, A. C. Potter, A. Vishwanath, *et al.*, Observation of a discrete time crystal, *Nature* **543**, 217 (2017).
- [11] S. Choi, J. Choi, R. Landig, G. Kucsko, H. Zhou, J. Isoya, F. Jelezko, S. Onoda, H. Sumiya, V. Khemani, *et al.*, Observation of discrete time-crystalline order in a disordered dipolar many-body system, *Nature* **543**, 221 (2017).
- [12] T. Li, Z.-X. Gong, Z.-Q. Yin, H. Quan, X. Yin, P. Zhang, L.-M. Duan, and X. Zhang, Space-time crystals of trapped ions, *Physical Review Letters* **109**, 163001 (2012).
- [13] D. V. Else, B. Bauer, and C. Nayak, Floquet time crystals, *Physical Review Letters* **117**, 090402 (2016).
- [14] S. Autti, V. Eltsov, and G. Volovik, Observation of a time quasicrystal and its transition to a superfluid time crystal, *Physical Review Letters* **120**, 215301 (2018).
- [15] J. Smits, L. Liao, H. Stoof, and P. van der Straten, Observation of a space-time crystal in a superfluid quantum gas, *Physical Review Letters* **121**, 185301 (2018).
- [16] A. Pizzi, A. Nunnenkamp, and J. Knolle, Bistability and time crystals in long-ranged directed percolation, *Nature communications* **12**, 1061 (2021).
- [17] S. Autti, P. J. Heikkinen, J. T. Mäkinen, G. E. Volovik, V. V. Zavjalov, and V. B. Eltsov, Ac josephson effect between two superfluid time crystals, *Nature Materials* **20**, 171 (2021).
- [18] N. Träger, P. Gruszecki, F. Lisiecki, F. Groß, J. Förster, M. Weigand, H. Glowinski, P. Kuświk, J. Dubowik, G. Schütz, *et al.*, Real-space observation of magnon interaction with driven space-time crystals, *Physical Review Letters* **126**, 057201 (2021).
- [19] H. Watanabe and M. Oshikawa, Absence of quantum time crystals, *Physical Review Letters* **114**, 251603 (2015).
- [20] A. Syrwid, J. Zakrzewski, and K. Sacha, Time crystal behavior of excited eigenstates, *Physical Review Letters* **119**, 250602 (2017).
- [21] B. Huang, Y.-H. Wu, and W. V. Liu, Clean floquet time crystals: models and realizations in cold atoms, *Physical Review Letters* **120**, 110603 (2018).
- [22] Z. Gong, R. Hamazaki, and M. Ueda, Discrete time-crystalline order in cavity and circuit qed systems, *Physical Review Letters* **120**, 040404 (2018).
- [23] N. Y. Yao, C. Nayak, L. Balents, and M. P. Zaletel, Classical discrete time crystals, *Nature Physics* **16**, 438 (2020).
- [24] F. Gambetta, F. Carollo, M. Marcuzzi, J. Garrahan, and I. Lesanovsky, Discrete time crystals in the absence of manifest symmetries or disorder in open quantum systems, *Physical Review Letters* **122**, 015701 (2019).
- [25] F. Machado, Q. Zhuang, N. Y. Yao, and M. P. Zaletel, Absolutely stable time crystals at finite temperature, *Physical Review Letters* **131**, 180402 (2023).
- [26] J. Rovny, R. L. Blum, and S. E. Barrett, Observation of discrete-time-crystal signatures in an ordered dipolar many-body system, *Physical Review Letters* **120**, 180603 (2018).
- [27] J. Randall, C. Bradley, F. van der Grienden, A. Galicia, M. Abobeih, M. Markham, D. Twitchen, F. Machado, N. Yao, and T. Taminiau, Many-body-localized discrete time crystal with a programmable spin-based quantum simulator, *Science* **374**, 1474 (2021).
- [28] W. W. Ho, S. Choi, M. D. Lukin, and D. A. Abanin, Critical time crystals in dipolar systems, *Physical Review Letters* **119**, 010602 (2017).
- [29] H. Keßler, P. Kongkhambut, C. Georges, L. Mathey, J. G. Cosme, and A. Hemmerich, Observation of a dissipative time crystal, *Physical Review Letters* **127**, 043602 (2021).
- [30] D. Vu and S. D. Sarma, Dissipative prethermal discrete time crystal, *Physical Review Letters* **130**, 130401 (2023).
- [31] A. Kyprianidis, F. Machado, W. Morong, P. Becker, K. S. Collins, D. V. Else, L. Feng, P. W. Hess, C. Nayak, G. Pagano, *et al.*, Observation of a prethermal discrete

- time crystal, *Science* **372**, 1192 (2021).
- [32] A. Pizzi, J. Knolle, and A. Nunnenkamp, Periodic discrete time crystals and quasicrystals with ultracold bosons, *Physical Review Letters* **123**, 150601 (2019).
- [33] A. Pizzi, J. Knolle, and A. Nunnenkamp, Higher-order and fractional discrete time crystals in clean long-range interacting systems, *Nature Communications* **12**, 2341 (2021).
- [34] D. Ding, Z. Bai, Z. Liu, B. Shi, G. Guo, W. Li, and C. S. Adams, Ergodicity breaking from rydberg clusters in a driven-dissipative many-body system, *Science Advances* **10**, ead15893 (2024).
- [35] K. Wadenpuhl and C. S. Adams, Emergence of synchronization in a driven-dissipative hot Rydberg vapor, *Physical Review Letters* **131**, 143002 (2023).
- [36] X. Wu, Z. Wang, F. Yang, R. Gao, C. Liang, M. K. Tey, X. Li, T. Pohl, and L. You, Observation of a dissipative time crystal in a strongly interacting Rydberg gas, *arXiv preprint arXiv:2305.20070* (2023).
- [37] B. Liu, L.-H. Zhang, Z.-K. Liu, J. Zhang, Z.-Y. Zhang, S.-Y. Shao, Q. Li, H.-C. Chen, Y. Ma, T.-Y. Han, *et al.*, Bifurcation of time crystals in driven and dissipative Rydberg atomic gas, *arXiv preprint arXiv:2402.13644* (2024).
- [38] B. Liu, L.-H. Zhang, Z.-K. Liu, J. Zhang, Z.-Y. Zhang, S.-Y. Shao, Q. Li, H.-C. Chen, Y. Ma, T.-Y. Han, *et al.*, Higher-order and fractional discrete time crystals in floquet-driven Rydberg atoms, *arXiv preprint arXiv:2402.13657* (2024).
- [39] M. Hajdušek, P. Solanki, R. Fazio, and S. Vinjanampathy, Seeding crystallization in time, *Physical Review Letters* **128**, 080603 (2022).
- [40] L.-H. Zhang, Z.-K. Liu, B. Liu, Z.-Y. Zhang, G.-C. Guo, D.-S. Ding, and B.-S. Shi, Rydberg microwave-frequency-comb spectrometer, *Physical Review Applied* **18**, 014033 (2022).
- [41] B. Liu, L.-H. Zhang, Z.-K. Liu, Z.-Y. Zhang, Z.-H. Zhu, W. Gao, G.-C. Guo, D.-S. Ding, and B.-S. Shi, Highly sensitive measurement of a megahertz rf electric field with a Rydberg-atom sensor, *Physical Review Applied* **18**, 014045 (2022).
- [42] N. Šibalić, J. D. Pritchard, C. S. Adams, and K. J. Weatherill, Arc: An open-source library for calculating properties of alkali Rydberg atoms, *Computer Physics Communications* **220**, 319 (2017).

## METHODS

### Experimental Setup

The system is based on the room temperature Caesium atoms in a 7-cm vapor cell. A three-photon excitation scheme is used to excite atoms from the ground state to the Rydberg state [38], in which a 852 nm probe field drives the transition of  $|6S_{1/2}\rangle \rightarrow |6P_{3/2}\rangle$ , a 1470 nm laser drives the transition of  $|6P_{3/2}\rangle \rightarrow |7S_{1/2}\rangle$ , and a 780 nm coupling field drives the transition of  $|7S_{1/2}\rangle \rightarrow |49P_{3/2}\rangle$ . In the experimental setup, the 852 nm laser beam is divided into two probe beams (one is probe and another is reference) to pass through the vapor cell ( $1/e^2$ -waist radius of approximately 200  $\mu\text{m}$ ), and

the 1470 nm and 780 nm laser beams propagate in the opposite direction to one of the probe laser beams to reduce the Doppler broadening effect. The 1470 nm and 780 nm laser beams have  $1/e^2$ -waist radius of approximately 500  $\mu\text{m}$ . These configurations induce three-photon electromagnetically induced transparency, leading to the transparency of the probe laser beam. Finally, the two 852 nm laser beams are received by a balanced photoelectric detector for differential amplification measurement.

The RF-field is applied by two parallel round electrode plates, which are placed parallel to each other on both sides of the vapor cell 4 cm apart. The positive and negative electrode plates are connected to a functional generator (F1), which is triggered by another functional generator (F2). The seed field is in microwave band that is generated from a vector signal source (Ceyear, 1465F-V), which is switched by the functional generator (F2). The seed field is fed through an external antenna to drive the transition of  $|R_2\rangle \rightarrow |R_3\rangle$  (the corresponding transition  $|49P_{3/2}\rangle \rightarrow |48D_{5/2}\rangle$  has a frequency of 6.507 GHz) with Rabi frequency  $\Omega_{\text{MW}}$ . The seed field couples the atoms at Rydberg state  $49P_{3/2}$  calculated by the Python package, Alkali Rydberg calculator [42]. The external antenna has a radiated direction that is perpendicular to the laser beam propagation direction. All data in the experiment are the signal in time domain, we make a Fourier transformation to measure the frequency of time crystal.

### Quantum Master Equation

To simulate the dynamics of seeding time crystal, we build a quantum many-body system by considering  $N$  four-level atoms composed of a ground state  $|g\rangle$  and three Rydberg states  $|R_1\rangle, |R_2\rangle, |R_3\rangle$  (all with an equal decay rate  $\gamma$ ). A laser excite atoms from  $|g\rangle$  to  $|R_1\rangle$  and  $|R_2\rangle$  with Rabi frequency  $\Omega_1$  and  $\Omega_2$  respectively. The microwave coupling the Rydberg states  $|R_2\rangle$  and  $|R_3\rangle$  with Rabi frequency  $\Omega_3(t)$ , where  $\Omega_3(t) = A_0 + A\text{Sin}(2\pi f_s t + \varphi_0 + \varphi)$  is the seed to drive system. The periodical RF-field driving shift the detuning  $\Delta(t)$ , which provides the Floquet-driven conditions. The excited Rydberg atoms interact strongly through the van der Waals interaction  $V_{ij} = C_6/|\mathbf{r}_i - \mathbf{r}_j|^6$ , here  $\mathbf{r}_i$  and  $\mathbf{r}_j$  are the locations of  $i$ -th and  $j$ -th atoms. The Hamiltonian of system is described as Eq.1, the dynamics of system is governed by the quantum master equation:

$$\partial_t \hat{\rho} = i[\hat{H}, \hat{\rho}] + \mathcal{L}_{R_1}[\hat{\rho}] + \mathcal{L}_{R_2}[\hat{\rho}] + \mathcal{L}_{R_3}[\hat{\rho}] \quad (2)$$

The Lindblad operators are given by  $\mathcal{L}_r = (\gamma/2) \sum_i (\hat{\sigma}_i^{r,g} \hat{\rho} \hat{\sigma}_i^{gr} - \{\hat{n}_i^r, \hat{\rho}\})$ , which represents the decay process from the Rydberg state  $|r\rangle$  ( $r = R_1, R_2, R_3$ ) to the ground state  $|g\rangle$ . As the thermal motion with large number of Rydberg atoms in system, the many-body correlation may be weak and we can consider the mean-field approximations. In the mean-field treatment,



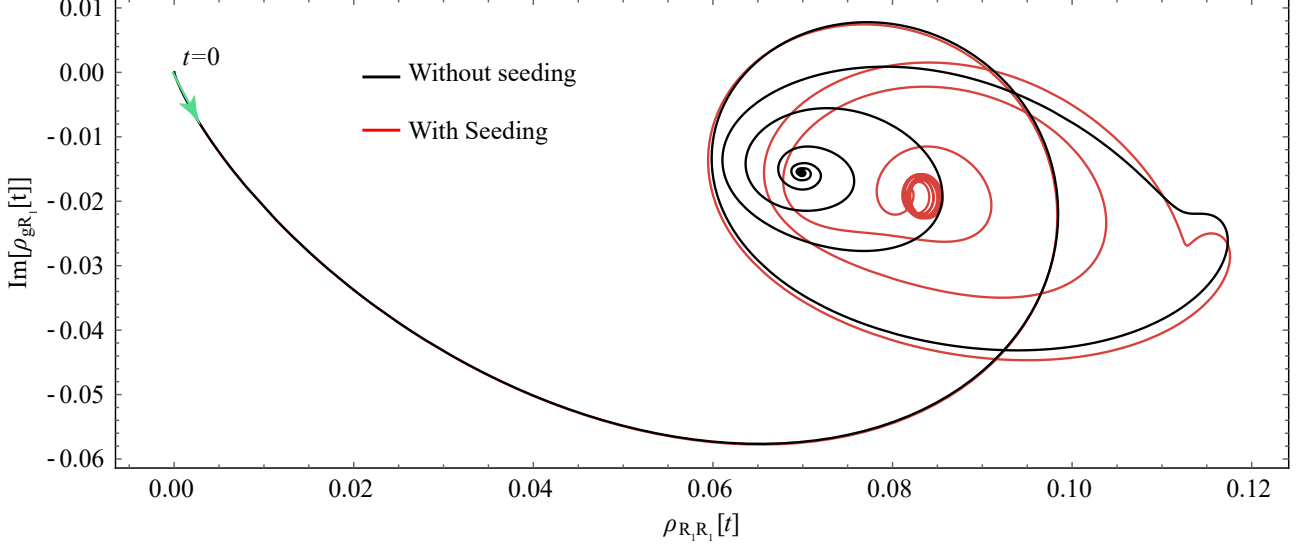


Figure 6. **The calculated phase plane in the basis of  $\rho_{R_1 R_1}$  and  $\text{Im}[\rho_{g R_1}]$  versus time  $t$ .** The black and red curves are the trajectories of the atoms at frequency of 2-DTC without and with seeding. There is an oscillation behavior with presence of seeding, see the persistent red cycles. While for no seeding, the atoms end a fixed black point. The green arrow indicates the initial state at  $t = 0$ . In these cases, the theoretical parameters are  $\chi = -22$ ,  $\Omega_1 = 3.5$ ,  $\Omega_2 = 3.5$ ,  $\gamma = 0.78$ ,  $\delta = 8.6$ ,  $A_0 = A = 1.5$ . The responses are filtered out by a low-pass filter which allows signals with frequencies below a certain cutoff frequency to pass through while attenuating higher frequencies.

we obtained the following equations:

$$\begin{aligned} \rho'_{g R_1}(t) &= \frac{1}{2}(-\gamma \rho_{g R_1}(t) + 2i(\Delta(t) - V_{\text{MF}})\rho_{g R_1}(t)) \\ &+ \frac{1}{2}\Omega_1 i \rho_{R_1 R_1}(t) - \frac{1}{2}\Omega_1 i \rho_{g g}(t) \\ &+ \frac{1}{2}i\Omega_2 \rho_{R_2 R_1}(t) - \frac{1}{2}i\Omega_3(t)\rho_{g R_3}(t), \end{aligned} \quad (3)$$

$$\begin{aligned} \rho'_{g R_2}(t) &= \frac{1}{2}(-\gamma + 2i\delta)\rho_{g R_2}(t) + i(\Delta(t) - V_{\text{MF}})\rho_{g R_2}(t) \\ &+ \frac{1}{2}i\Omega_1 \rho_{R_1 R_2}(t) + \frac{1}{2}\Omega_2(i\rho_{R_2 R_2}(t) - i\rho_{g g}(t)), \end{aligned} \quad (4)$$

$$\begin{aligned} \rho'_{g R_3}(t) &= \frac{1}{2}(-\gamma + 2i\delta)\rho_{g R_3}(t) + i(\Delta(t) - V_{\text{MF}})\rho_{g R_3}(t) \\ &+ \frac{1}{2}i\Omega_1 \rho_{R_1 R_3}(t) + \frac{1}{2}i\Omega_2 \rho_{R_2 R_3}(t) - \frac{1}{2}i\Omega_3(t)\rho_{g R_1}(t), \end{aligned} \quad (5)$$

$$\begin{aligned} \rho'_{R_1 R_1}(t) &= -\gamma \rho_{R_1 R_1}(t) + \frac{1}{2}\Omega_1(i\rho_{g R_1}(t) - i\rho_{R_1 g}(t)) \\ &+ \frac{1}{2}\Omega_3(t)(i\rho_{R_3 R_1}(t) - i\rho_{R_1 R_3}(t)), \end{aligned} \quad (6)$$

$$\begin{aligned} \rho'_{R_1 R_2}(t) &= \frac{1}{2}(-2\gamma \rho_{R_1 R_2}(t) + 2i\delta \rho_{R_1 R_2}(t)) + \frac{1}{2}i\Omega_1 \rho_{g R_2}(t) \\ &- \frac{1}{2}i\Omega_2 \rho_{R_2 g}(t) + \frac{1}{2}i\Omega_3(t)\rho_{R_3 R_2}(t), \end{aligned} \quad (7)$$

$$\begin{aligned} \rho'_{R_1 R_3}(t) &= \frac{1}{2}(-2\gamma \rho_{R_1 R_3}(t) + 2i\delta \rho_{R_1 R_3}(t)) + \frac{1}{2}i\Omega_1 \rho_{g R_3}(t) \\ &+ \frac{1}{2}\Omega_3(t)(i\rho_{R_3 R_3}(t) - i\rho_{R_1 R_1}(t)), \end{aligned} \quad (8)$$

$$\rho'_{R_2 R_2}(t) = -\gamma \rho_{R_2 R_2}(t) + \frac{1}{2}\Omega_2(i\rho_{g R_2}(t) - i\rho_{R_2 g}(t)), \quad (9)$$

$$\rho'_{R_2 R_3}(t) = -\gamma \rho_{R_2 R_3}(t) + \frac{1}{2}i\Omega_2 \rho_{g R_3}(t) - \frac{1}{2}i\Omega_3(t)\rho_{R_2 R_1}(t), \quad (10)$$

$$\rho'_{R_3 R_3}(t) = -\gamma \rho_{R_3 R_3}(t) + \frac{1}{2}\Omega_3(t)(i\rho_{R_1 R_3}(t) - i\rho_{R_3 R_1}(t)) \quad (11)$$

where  $V_{\text{MF}} = \chi(\rho_{R_1 R_1}(t) + \rho_{R_2 R_2}(t) + \rho_{R_3 R_3}(t))$  is the mean-field shift of Rydberg atoms.

### Trajectories in Phase Plane

By numerically calculating the master equation, we can obtain the time evolution of the system. We apply a low-pass filter to the atomic density matrices  $\rho_{R_1 R_1}$  and  $\rho_{g R_1}$ , effectively removing the oscillating signals at frequency  $f = f_0$ . By this way, we plot the phase plane in the basis of  $\rho_{R_1 R_1}$  and  $\rho_{g R_1}$  versus time  $t$ , as shown in Fig. 6, which allows us to reveal how the behavior of the system has changed with or without the seed field. We set the condition of the system before the critical point [ $\delta_c = 8.7$ ], for example  $\delta = 8.6$ . At the beginning, the trajectories of the atoms are the same for both cases with and without seeding. However, as time progresses, the trajectories bifurcate and take different paths in the phase plane, see the black and red trajectories in Fig. 6.

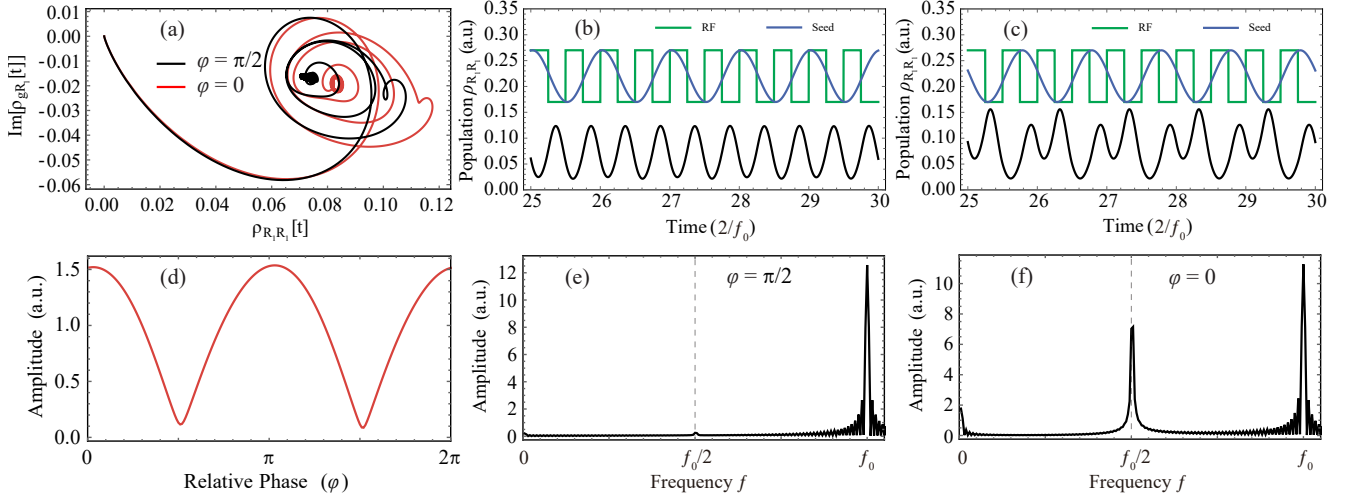


Figure 7. **The phase dependent seeding.** (a) represents the phase plane of atoms, including trajectories with relative phases  $\varphi = \pi/2$  (black) and  $\varphi = 0$  (red). (b) and (c) correspond to time flow of Rydberg population  $\rho_{R_1 R_1}$  at  $\varphi = \pi/2$  and  $\varphi = 0$ , respectively. The green and blue curves are the waveform of the RF-driving field and seed field. In these cases, the theoretical parameters are  $\chi = -22$ ,  $\Omega_1 = 3.5$ ,  $\Omega_2 = 3.5$ ,  $\gamma = 0.78$ ,  $\delta = 8.6$ ,  $A_0 = A = 1.5$ . (d) The calculated amplitude of the seeded 2-DTC versus the relative phase  $\varphi$ . In this case,  $A_0 = 0.5$ ,  $A = 1.0$ . (e) and (f) The calculated Fourier spectrum with a relative phase  $\varphi = \pi/2$  and  $\varphi = 0$ .

In the absence of a seed field, all atoms converge to a relatively fixed point in the phase plane, indicating that they do not exhibit 2-DTC oscillation behavior. On the other hand, when a seed field is applied, all atoms exhibit collective dynamics and show persistent oscillating trajectories, forming a limit cycle [34]. The frequency of these oscillations is  $f = f_0/2$  with same with the seed field, revealing the periodical features of seeded 2-DTC. This shows the dynamic behavior of system with and without seeding.

### Phase-Dependent Seeding

The theoretical simulations show that the relative phase between the seed field and the RF-field also affects strength of the seeded 2-DTC. We map the phase plane at  $\varphi = \pi/2$  and  $\varphi = 0$  as shown in Fig. 7(a), in which the phase difference leads to the different trajectories and the distinct cycling size. Figures. 7(b) and (c) are the corresponding configurations of time sequences. The different time sequences result in a distinct joint action on exciting Rydberg population  $\rho_{R_1 R_1}$ . By altering the relative phase  $\varphi$ , we record the amplitude of the seeded 2-DTC and plot the results shown in Fig. 7(d). We can find that the periodicity of the seed 2-DTC is twice of the RF-field driving, which is in good agreement with the experimental observations [see Fig. 3(b)]. By setting  $\varphi = \pi/2$  and  $\varphi = 0$ , we obtain the two opposite situations of synchronization and unsynchronization, as given in Fig. 7(e) and Fig. 7(f), respectively.

Once the initial conditions are fixed by setting the initial phase  $\varphi_0 = 0.93\pi$ , the phase difference between the

driving field and the seed field is directly related to the amplification of 2-DTC order. When the waveform of the seed field is in phase with the 2-DTC [it means that the driving and seed fields have the same timing with  $\varphi = 0$ ], the atoms are gradually synchronized, the signal of 2-DTC will be further amplified. When the waveform of the seed field is out of phase with the 2-DTC [ $\varphi = \pi/2$ ], the atoms are not synchronized, and the signal 2-DTC cannot be effectively amplified. These result in an obvious difference on response of 2-DTC, see the height of peaks at  $f = f_0/2$  in the Fourier spectrum given in Fig. 7(e) and Fig. 7(f).

### Seeding Fractional DTCs

We also perform numerical studies on the emergence of seeded  $n$ -DTCs with  $n$  beyond integers. In these studies, we input a seed field with frequencies  $f_s = 0.475f_0$  and  $f_s = 0.45f_0$  which are not resonant with the fundamental frequency of 2-DTC ( $f = f_0/2$ ). We then record the corresponding Fourier spectrum of the Rydberg population  $\rho_{R_1 R_1}$ . The Fourier spectrum are shown in Fig. 8(a) and Fig. 8(b), in which we observe the seeded  $n$ -DTCs with fractional numbers  $n = 40/19$  and  $n = 20/9$  respectively. These numerical studies show prediction for seeding  $n$ -DTCs with fractional values of  $n$ .

In the experiment, we applied a seed field with frequencies of  $f_s = 2\pi \times 19$  kHz and  $f_s = 2\pi \times 18$  kHz. We then measured the Fourier spectrum of probe transmission and found that the measured results are consistent with the theoretical predictions, as shown in Fig. 8(c) and Fig. 8(d). In these two results, the peaks marked

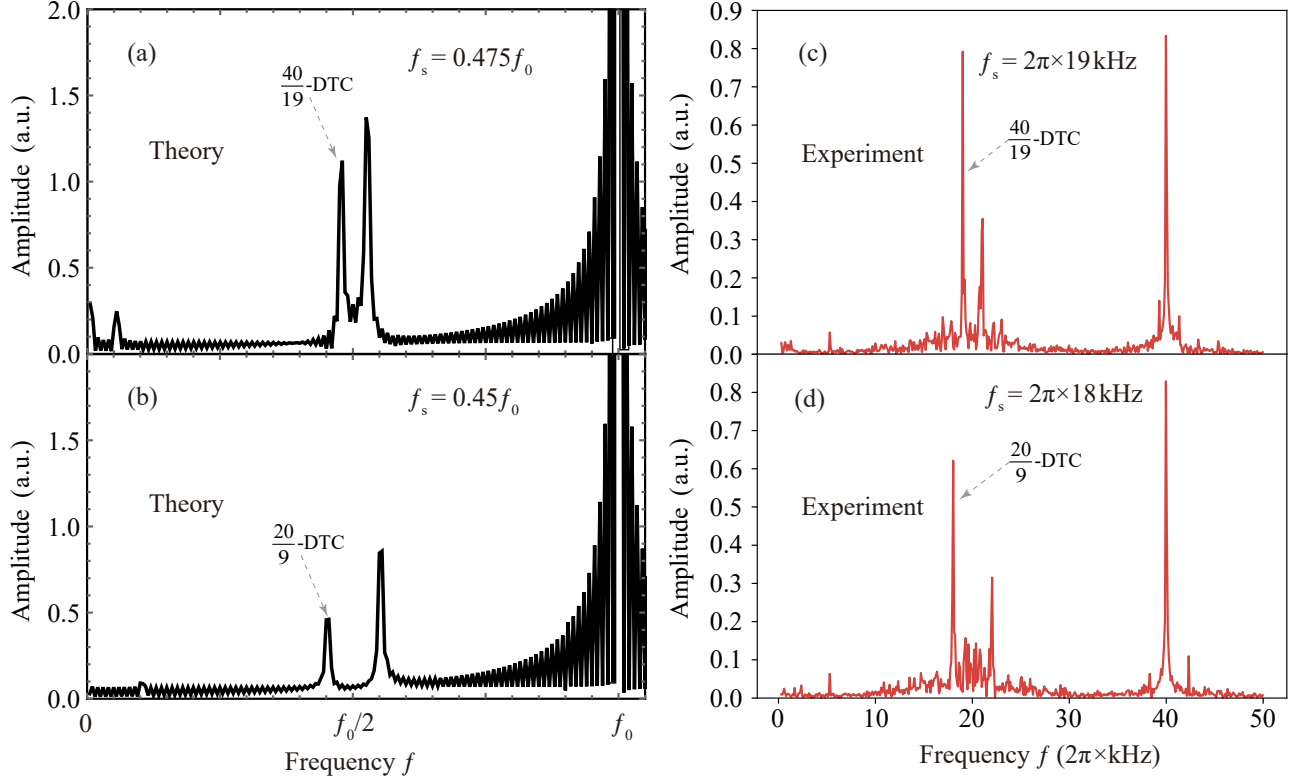


Figure 8. **Seeding fractional DTCs.** (a) and (b) are the calculated results of seeding fractional DTCs by altering the seed frequencies of  $f_s = 0.475f_0$  and  $f_s = 0.45f_0$ . The peaks [marked by the arrow of dotted lines] in the Fourier spectrum correspond to the subharmonic responses of 40/19-DTC and 20/9-DTC. In these cases, the theoretical parameters are  $\chi = -22$ ,  $\Omega_1 = 3.5$ ,  $\Omega_2 = 3.5$ ,  $\gamma = 0.78$ ,  $\delta = 8.6$ ,  $A_0 = A = 1.2$ . (c) and (d) are the measured data by applying the seed field with frequencies of  $f_s = 2\pi \times 19$  kHz and  $f_s = 2\pi \times 18$  kHz. The measured fractional DTCs (40/19-DTC and 20/9-DTC) are found by the marked peaks in the Fourier spectrum. The symmetric peaks on the other sides are the difference frequency signals, which has a frequency of  $f_0 - f_s$ .

by the dotted arrows in the Fourier spectrum correspond to the seeded fractional DTCs (40/19-DTC and 20/9-DTC). Both of theoretical and experimental findings suggest that fractional DTCs can be seeded by selecting the frequencies of the seed fields.

#### ACKNOWLEDGEMENTS

We acknowledge funding from the National Key R and D Program of China (Grant No. 2022YFA1404002), the National Natural Science Foundation of China (Grant Nos. U20A20218, 61525504, and 61435011), the Anhui Initiative in Quantum Information Technologies (Grant No. AHY020200), and the Major Science and Technology Projects in Anhui Province (Grant No.

202203a13010001).

#### AUTHOR CONTRIBUTIONS STATEMENT

D.-S.D. conceived the idea for the study. B.L. conducted the physical experiments and developed the theoretical model. The manuscript was written by D.-S.D and B.L. The research was supervised by D.-S.D. All authors contributed to discussions regarding the results and the analysis contained in the manuscript.

#### COMPETING INTERESTS

The authors declare no competing interests.